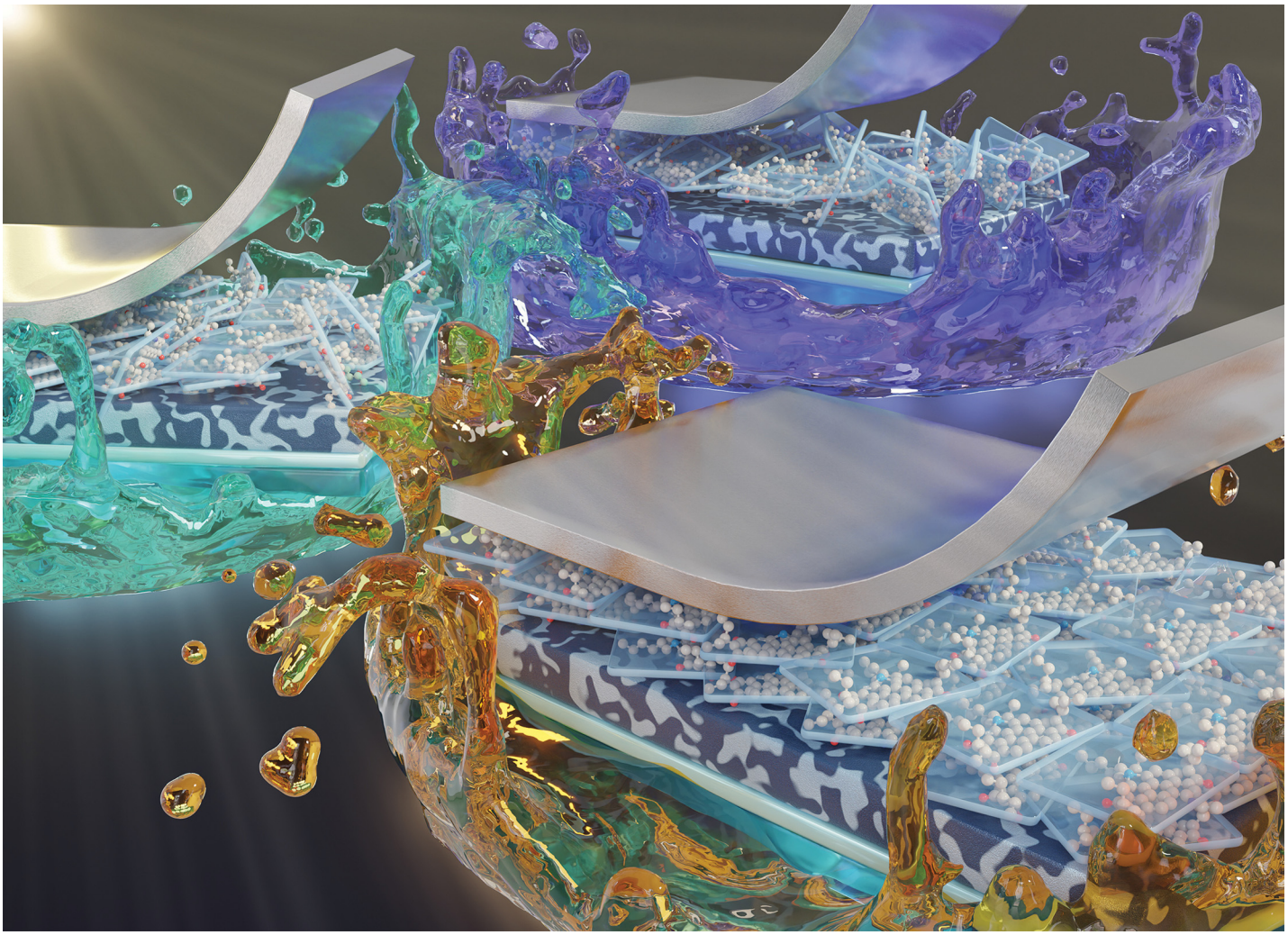

Showing research conducted by the Doumon Group, Department of Materials Science and Engineering, The Pennsylvania State University, United States.

Chemical structure and processing solvent of cathode interlayer materials affect organic solar cells performance

The team investigates the effect of chemical structure and processing solvents of PDINO and F-PDIN-EH, perylene diimide-based cathode interlayer materials, on the efficiency and long-term stability of organic solar cells. By comparing a new fluorinated material, F-PDIN-EH, in solvents with different polarity to the widely used PDINO, the chemical structure and solvent-dependent degradation mechanisms were highlighted. Their findings provide critical insights into achieving sustainable and stable organic photovoltaics using eco-friendly processing strategies.

As featured in:

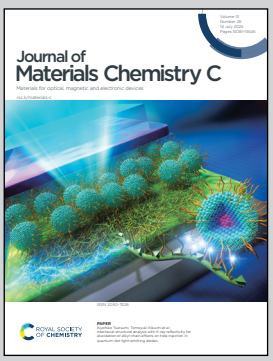

See Nutifafa Y. Doumon *et al.*, *J. Mater. Chem. C*, 2025, **13**, 13131.

ROYAL SOCIETY OF CHEMISTRY

rsc.li/materials-c

Registered charity number: 207890

Journal of Materials Chemistry C

ROYAL SOCIETY OF CHEMISTRY

PAPER

View Article Online
View Journal | View Issue

Cite this: J. Mater. Chem. C, 2025, 13, 13131

Chemical structure and processing solvent of cathode interlayer materials affect organic solar cells performance†

Souk Y. Kim,[a] Pimmada Sawangwong,[a] Colton Atkinson,[b] Gregory C. Welch[b] and Nutifafa Y. Doumon*[acd]

Interlayers in organic solar cells (OSCs) are crucial for efficient charge carrier transport and extraction. Recent research has introduced cathode interlayer (CIL) materials, which are soluble in polar, amphiphilic, and non-polar solvents. However, studies on how these solvents affect device performance, particularly stability under various conditions, remain limited. In this work, we investigate the effects of the chemical structure of a recently synthesized perylene diimide (PDI) CIL material, F-PDIN-EH, and its eco-friendly polar (methanol), amphiphilic (1-butanol), and non-polar (heptane) processing solvents, on device performance, compared to PDINO, a widely studied PDI-based CIL material. This is one of the first investigations into the effect of non-polar CIL processing solvents on device stability. OSC devices with F-PDIN-EH yield comparable efficiency to PDINO-based devices but are consistently less stable, irrespective of the solvent. Notably, the heptane-processed F-PIN-EH-based devices exhibit the lowest stability. We investigated the degradation mechanisms in the device and the interfaces through an in-depth study using TPV, TPC, extracted charge carrier density, and light intensity dependence of J_{sc} and V_{oc}. Further studies are conducted using absorption spectroscopy, FTIR, and mobility measurements to ascertain the source of degradation. The loss in performance over time, especially in the heptane-processed F-PIN-EH-based devices, is mainly due to increased surface recombination and imbalanced charge mobility. This study provides valuable insights into the dependency of device performance on the chemical structure and processing solvents of CIL materials. It also highlights challenges for sustainable, greener OSCs.

Received 10th January 2025,
Accepted 20th May 2025

DOI: 10.1039/d5tc00110b

rsc.li/materials-c

Introduction

Research in renewable energy has advanced significantly over the last decades, with solar energy and its harvesting technologies emerging as the most promising. Among these technologies, organic solar cells (OSCs) have garnered considerable attention due to their inherent advantages, including lightweight, flexibility, solution processability, and tunable material properties.[1–4] These unique properties position OSCs for a wide range of indoor and outdoor applications, such as agrivoltaics,[5–7] internet of things

[a] Department of Materials Science and Engineering, The Pennsylvania State University, University Park, PA 16802, USA. E-mail: nzd5349@psu.edu
[b] Department of Chemistry, University of Calgary, 2500 University Drive N.W., Calgary, Alberta T2N 1N4, Canada
[c] Department of Engineering Science and Mechanics, The Pennsylvania State University, University Park, PA 16802, USA
[d] Materials Research Institute, The Pennsylvania State University, University Park, PA 16802, USA

† Electronic supplementary information (ESI) available. See DOI: https://doi.org/10.1039/d5tc00110b

Nutifafa Y. Doumon

Nutifafa Y. Doumon is a Virginia S. and Philip L. Walker Jr professor and an assistant professor of Materials Science and Engineering & Engineering Science and Mechanics at The Pennsylvania State University. His research interest spans organic/polymer and halide perovskite semiconductors for indoor/outdoor photovoltaic and optoelectronic device fabrication/characterization, stability, and reliability testing. He was a postdoctoral fellow at NREL in Golden, Colorado, and INRS-EMT in Varennes, Canada. He holds a PhD and MSc in Nanoscience and an MA in Leadership from the University of Groningen, after an MSc and a BSc in Physics from AUST-Abuja and the University of Ghana, respectively.

(IoT) nodes,[8–10] and building-integrated photovoltaics (BIPV).[11–13] Consequently, research on OSCs has surged, leading to remarkable progress in power conversion efficiency (PCE), recently surpassing 20% for single-junction[14] and tandem structures[15,16] under 1 sun.

In line with this progress, Heliatek achieved a milestone by passing the IEC 61646 stability test, which evaluates the long-term performance of thin-film solar modules under standardized conditions.[17] This achievement underscores the growing commercial feasibility of OSCs. However, several challenges remain, including maintaining high efficiency and stability,[18–22] particularly when scaling up the production to large-area solar modules and ensuring that product costs are kept at a minimum for OSCs to be competitive in the current marketplace.

Unlike traditional PV and other next-generation PVs, one critical factor influencing the efficiency and stability of OSCs is interlayers, such as the anode interlayer and cathode interlayer (CIL). These layers play a key role in aligning the energy levels between the photoactive layer and the electrodes, reducing the energetic barrier. Such alignment minimizes charge carrier recombination and enhances charge extraction, improving device efficiency.[23–25] Many materials have been explored as interlayers, including metal oxides, conjugated polymers, and organic small molecules.[26–28] However, metal oxide-based CILs can chemically interact with bulk heterojunction (BHJ) materials, leading to stability issues in OSC devices.[29] Polymer-based CILs, on the other hand, often suffer from challenges related to complex synthesis, difficulties in purification, and inconsistencies in batch-to-batch reproducibility, which hinder their practical application in commercial OPV technologies.[29,30] In this context, π-conjugated small molecules, particularly perylene diimides (PDIs), have gained attention as promising CIL materials for OSC devices.[31,32] Their strong electron-withdrawing dicarboxylic imide groups and highly planar structures facilitate efficient charge transport by enabling tight intermolecular stacking, contributing to their high electron affinity and charge carrier mobility.[30] Additionally, PDIs exhibit remarkable photostability due to their extensive π-conjugation, stabilizing radical anions.[30] Their chemical structure is also highly tunable, allowing for fine adjustments in cathode work function modification through tailored molecular design. Accordingly, key CILs in recent high-performance OSCs are self-doped PDINO, PDIN, PDINN, *etc.*, from the perylene diimide (PDI) family of small molecules, a class of polycyclic aromatic hydrocarbon chromophores.[33–37]

Furthermore, self-doping in such materials enabled by the unpaired electrons in the aliphatic amine group of the PDI core enhances charge conductivity and CIL functionality.[34,38] However, the self-doping limits the processing solvent of such materials to highly polar solvents such as methanol (MeOH). The choice of solvents for solution-processed OSCs is crucial as they significantly affect the film formation, morphology, and interface properties, directly impacting the charge carrier transport and collection.[39] Nevertheless, research on the solvent effect has been largely limited to active layer solvents.[39] This is mainly because the choice of CIL solvents has traditionally been restricted to polar alcohol solvents, as they must be carefully selected to avoid dissolving and/or swelling the active layer.[40,41] Despite these constraints, Song *et al.*[42] conducted a study to investigate the impact of alcohol-based solvents. They compared devices without CILs, devices treated with alcohol solvent only, and devices with CILs dissolved in alcohol solvent.[42] Their result indicated that while solvent treatment alone slightly increased the efficiency, devices with CILs showed significantly enhanced efficiency. However, beyond this study, the role of CIL chemical structure and processing solvents in OSC performance remains unexplored, especially regarding stability.

Recently, Atkinson *et al.* synthesized a novel small molecule, F-PDIN-EH,[30] from the PDI family. This molecule can be soluble in various green solvents, exploring the range of solvent polarity: polar, amphiphilic, and non-polar.[30] While retaining relatively good conductivity and electron transfer properties when processed into thin films as its PDINO counterpart, this fluorinated *N*-annulated PDI material exhibits improved solubility across a range of solvents, including a 10-fold increase in the non-polar solvent, heptane (Hep), compared to its non-fluorinated derivatives, PDIN-EH and PDINO. This development is significant as it broadens the scope of materials and solvents available for CIL processing in OSCs. However, despite this important achievement, the direct impact of CIL solvents on OSC performance (efficiency and stability) has not yet been thoroughly explored.

Therefore, we investigate the effects of F-PDIN-EH as a CIL material, processed in various solvent nature, MeOH (polar), But (amphiphilic), and Hep (non-polar), on device performance, compared to commonly used PDINO processed in MeOH. We employ techniques such as transient photovoltage (TPV), transient photocurrent (TPC), and light-intensity-dependent V_{oc} and J_{sc} measurements to gain insights into charge carrier dynamics and recombination mechanisms in fresh and aged devices. We systematically evaluate shelf, thermal, and photo-induced stability under inert and ambient conditions following the international summit on organic photovoltaic stability (ISOS) protocols. These protocols, established to provide consistency and repeatability in the stability assessment and reporting procedures across laboratories, were introduced in 2011 for OSCs[43] and in 2020 for perovskite PVs.[44] Further technical details of the exact ISOS protocols (ISOS-D-1, ISOS-T-1, and ISOS-L-1) from the broader protocols are provided in the experimental section. These evaluations offer a more comprehensive understanding of how material properties and solvent choices influence the long-term performance of OSCs.

Results and discussions

Bulk heterojunction bilayer conventional OSC structures are fabricated, as depicted in Fig. 1(a). PM6 and Y6, commonly used high-performance donor and acceptor materials, are chosen as photoactive materials. Fig. 1(b) shows the differences in chemical structures of the CIL materials and their solvents. Replacing hydrogen with fluorine in F-PDIN-EH induces a dipole moment and localizes electron density around the fluorine atom.[30] This delocalization facilitates C–H···F interactions

between regions of varying electron density, contributing to the enhanced solubility of F-PDIN-EH in organic solvents, as supported by the Hansen solubility parameters.[30] Based on their CIL materials and processing solvents, devices are referred to as P-MeOH for PDINO in methanol, F-MeOH for F-PDIN-EH in methanol, F-But for F-PDIN-EH in 1-butanol, and F-Hep for F-PDIN-EH in heptane.

The *J*–*V* characteristics and PV parameters in Fig. S1 (ESI†), Fig. 1(c), and Table 1 show that P-MeOH-based devices achieve slightly higher PCE than F-PDIN-EH devices due mainly to their higher fill factor (FF). F-But devices exhibit comparable current density (J_{sc}) and FF with a slightly higher open-circuit voltage (V_{oc}) than P-MeOH devices. Similarly, F-Hep devices exhibit comparable J_{sc} and V_{oc}, though their FF is lower than P-MeOH and F-But devices. In contrast, F-MeOH devices show the lowest V_{oc} and FF. The reduced performance of F-MeOH is likely due to the limited solubility of F-PDIN-EH in MeOH, leading to aggregated particles with higher surface roughness, as seen in the AFM images of their fresh film in Fig. 2. In brief, F-PDIN-EH, without the self-doping capability, yields devices with comparable efficiency to PDINO devices.

To study the effect of CIL materials and their solvents on stability, we measured shelf (ISOS-D-1), thermal (ISOS-T-1), and photostability (ISOS-L-1) under ambient and nitrogen environments. Interestingly, the stability behavior of the devices with different CIL materials and solvents significantly varies, as shown in Fig. 3. While there are differences in stability behavior between PDINO and F-PDIN-EH due to their chemical structures, the distinct effects of solvents in the same material are particularly interesting. Fig. 3(a) shows the inert photostability at open circuit. Device lifetimes (T_{80}) are derived at 80% of the initial device PCE value. The P-MeOH-based devices exhibit a long lifetime beyond the 180 h measurement time, displaying superior stability to all devices with F-PDIN-EH. The lifetime of devices with F-MeOH, F-But, and F-Hep are 116 h, 153 h, and 78 h, respectively. F-But is the most stable among the F-PDIN-EH devices, followed by F-MeOH and F-Hep. With optimized conditions for the photoactive and other layers, we also noticed that optimizing the CILs' deposition conditions significantly affects the stability of the devices, irrespective of the CIL material or its processing solvent, as shown in Fig. S2 (ESI†). In particular, the devices with unoptimized F-series CILs degrade significantly faster under the same photostability test condition with lifetimes between 10 to 20 hours. This is in contrast to their efficiency, which varies insignificantly.

The ambient photostability in Fig. 3(b) shows a similar trend, as in Fig. 3(a) and Fig. S2 (ESI†), but a faster degradation rate with no significant differences in F-PDIN-EH-based devices (with T_{80} of 30 min for P-MeOH and between 6 to 9 min for F-based devices). The overall stability trend is similar for photostability and shelf stability under ambient and N_2 conditions, as shown in Fig. 3, Fig. S3, and S4 (ESI†). Thus, PDINO remains more stable than F-PIN-EH, and F-Hep records the worst stability under these conditions. The AFM images of the fresh and degraded films reveal increased surface roughness for all films from the fresh state to the degraded state except for F-Hep, which shows a reduced surface roughness with a difference of 0.03 nm. The bare PM6:Y6 surface roughness increased by 0.06 nm, while PM6:Y6/P-MeOH, PM6:Y6/F-MeOH, and PM6:Y6/F-But films increased by 0.34 nm, 0.01 nm, and 0.10 nm, respectively.

The thermal stability measurements of the devices in Fig. S5 and S6 (ESI†) reveal a much faster degradation rate than their photostability and shelf stability. Under nitrogen, in Fig. S5 (ESI†), the T_{80} values are less than 20 min for F-But and F-MeOH and less than 75 min for P-MeOH and F-Hep. In addition, the ambient thermal stability (Fig. S6, ESI†) highlights the effect of the differences in chemical structures of the CIL materials on the device stability more clearly, showing a much faster degradation of F-series devices compared to P-MeOH mainly due to a loss in V_{oc}.

We first probe the observed influence of CIL material and their solvents on the charge carrier dynamics by studying charge carrier recombination behavior *via* transient photovoltage (TPV) and transient photocurrent (TPC) measurements.[45,46] The recombination mechanisms vary with light intensity. At a higher light intensity, there are higher densities of charge carriers; thus, bimolecular recombination generally dominates, while trap-assisted recombination dominates at a lower light intensity. Therefore, different light intensities are strategically used for TPV and TPC. Photovoltage decay is a function of excessive photocarrier density, which decreases faster with higher charge carrier recombination.[47,48] Fig. 4(a) and (b) show the decay of normalized voltage with a biexponential decay behavior of fresh and degraded devices. The carrier lifetime is

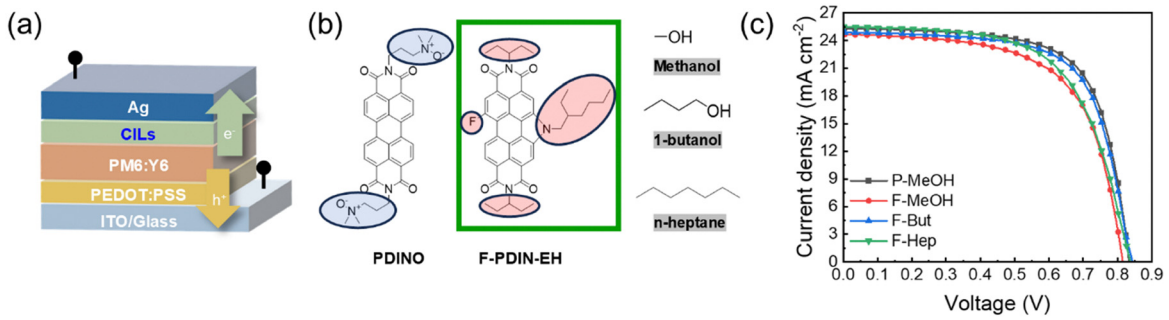

Fig. 1 (a) Schematic of the conventional structure of PM6:Y6 OSCs highlighting the CIL layer with (b) displaying the chemical structure of the CIL materials and the processing solvents. (c) *J*–*V* curves of the PM6:Y6 OSCs with different CILs.

Table 1 PV parameters of the J–V characteristics (Fig. 1(c)) of the ITO/PEDOT:PSS/PM6:Y6/CILs/Ag devices, as shown in (Fig. 1(a)). The average of J–V parameters is calculated from at least 10 to 15 devices

#	CILs	J_{sc} (mA cm^{-2})	V_{oc} (V)	FF (%)	PCE (%)
1	P-MeOH	25.32 (24.87 ± 0.51)	0.83 (0.84 ± 0.01)	68.4 (67.9 ± 1.0)	14.4 (14.1 ± 0.2)
2	F-MeOH	24.67 (24.21 ± 0.42)	0.81 (0.81 ± 0.01)	62.5 (62.1 ± 0.8)	12.6 (12.2 ± 0.2)
3	F-But	24.89 (24.24 ± 0.44)	0.84 (0.84 ± 0.01)	67.1 (67.3 ± 0.7)	14.0 (13.6 ± 0.3)
4	F-Hep	25.50 (24.12 ± 1.20)	0.85 (0.83 ± 0.02)	60.0 (59.9 ± 1.1)	13.1 (12.1 ± 0.9)

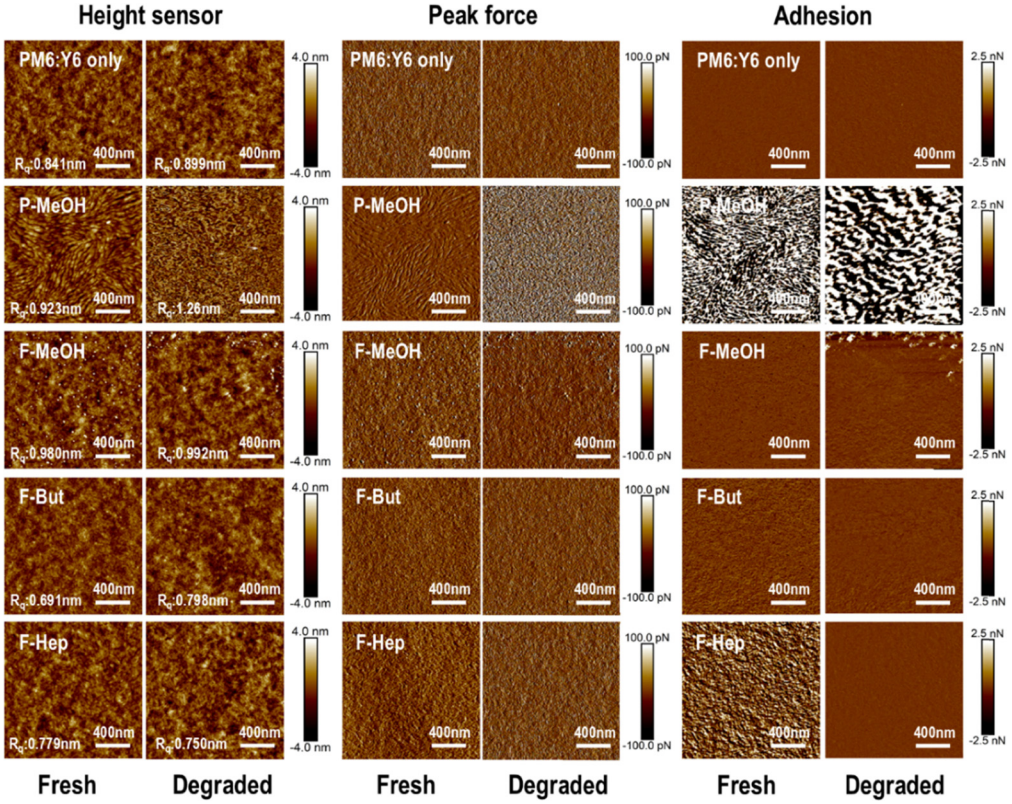

Fig. 2 Atomic force microscope (AFM) images of fresh and degraded (stored for 550 h under N_2 environment) PM6:Y6/CILs films, showing the height sensor, peak force, and adhesion images: top row (pristine PM6:Y6 film), second row (PM6:Y6/P-MeOH film), third row (PM6:Y6/F-MeOH film), fourth row (PM6:Y6/F-But film), and last row (PM6:Y6/F-Hep film).

obtained by fitting the TPV curve to a bi-exponential function. The detailed values and equations for TPV are provided in Table S1 (ESI†). The carrier lifetimes for the fresh devices of P-MeOH, F-MeOH, F-But, and F-Hep are 22.6, 24.9, 30.8, and 28.5 μs, respectively. F-But and F-Hep exhibit higher charge carrier lifetime, although their PCEs are lower than that of P-MeOH, which can be attributed to the smoother surfaces of F-But and F-Hep, as observed in AFM images (Fig. 2). These smoother surfaces can be ascribed to the higher boiling points of But (117.7 °C) and Hep (98.4 °C), which leads to slow evaporation after deposition compared to fast evaporation with volatile methanol (64.7 °C). However, the charge carrier lifetime of P-MeOH exhibits significantly higher values than the F-series devices after 55 hours under illumination (with a slight increase for F-But and a notable decrease for F-MeOH and F-Hep), indicating much lower non-geminate recombination, particularly trap-assisted recombination. This is consistent with and can be explained by the trend observed in the overall mobility change in fresh compared to degraded devices, as shown in Fig. S7 (ESI†). That is an increase in mobility for P-MeOH upon degradation, a slight decrease for F-But, followed by notable decreases for F-MeOH and F-Hep.

Next, we investigate the effect of CILs on charge extraction using transient photocurrent (TPC) decay. The photocurrent decay reflects photocarrier extraction dynamics and slows down with increased charge carrier recombination.[45,49] Fig. 4(c) and (d) present the photocurrent decay of the fresh and degraded devices with different CILs, respectively. The calculated decay times are summarized in Table S2 (ESI†). Consistent with the previous measurements, the fresh P-MeOH and F-But devices exhibit shorter charge extraction times, indicating lower charge carrier recombination. Interestingly, the F-MeOH fresh device also shows relatively low charge extraction times, indicating its

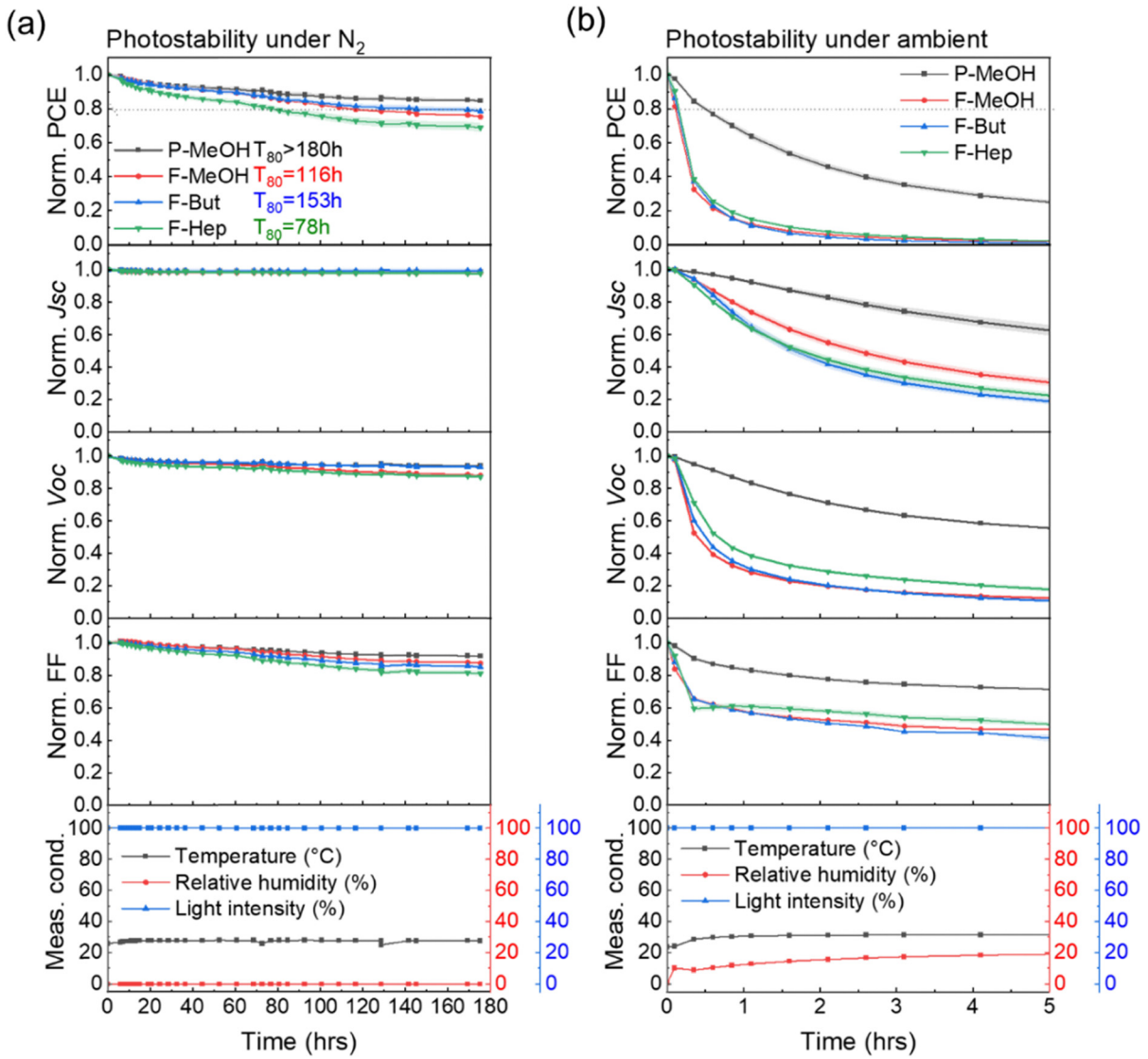

Fig. 3 Photostability measurement (a) under N_2 for over 170 hours and (b) in ambient for 5 hours (more than 5 devices each): the top four graphs are normalized PCE, J_{sc}, V_{oc}, and FF, and the bottom graph represents the measurement conditions (temperature, relative humidity, and light intensity).

relatively lower trap-assisted recombination, while the F-Hep fresh device demonstrates significantly higher charge extraction time. The degraded P-MeOH and F-MeOH devices maintain almost the same charge extraction times as their fresh devices, whereas F-But and F-Hep show increased values. This finding highlights the solvent effect of CILs, independent of the material. Although smooth films are formed with But and Hep, as seen in the AFM images in Fig. 2, the charge extraction times increased after degradation. Notably, the discrepancy between slow (τ_1) and fast (τ_2) decay times in F-Hep suggests a much higher recombination mechanism than the rest, explaining their low FF at the fresh state and its rapid degradation upon exposure due to an imbalance in charge mobility/transport as suggested by their overall charge and electron mobility measurements.[20,50–52]

To validate the TPV and TPC measurements, we further analyze the extracted charge carrier density as a function of light intensity, as shown in Fig. 4(e) and (f). P-MeOH and F-But exhibit higher charge carrier density extraction in the fresh samples, consistent with earlier results. F-MeOH demonstrates similar charge extraction to F-But in the lower light intensity region, indicating lower trap-assisted recombination; however, it decreases in the higher light intensity region due to increased bimolecular recombination. Conversely, F-Hep exhibits lower charge extraction in the lower light intensity region, attributed to higher trap-assisted recombination, while achieving higher charge carrier density extraction in the higher light intensity region, reflecting reduced bimolecular recombination. These results align with the previous discussions in TPV and TPC. In the degraded devices, as shown in Fig. 4(f), the extracted charge carrier density significantly decreases across all the samples, with a significant drop in the bimolecular region. Notably, F-But retains higher charge extraction in the lower light intensity region, indicating lower trap-assisted recombination.

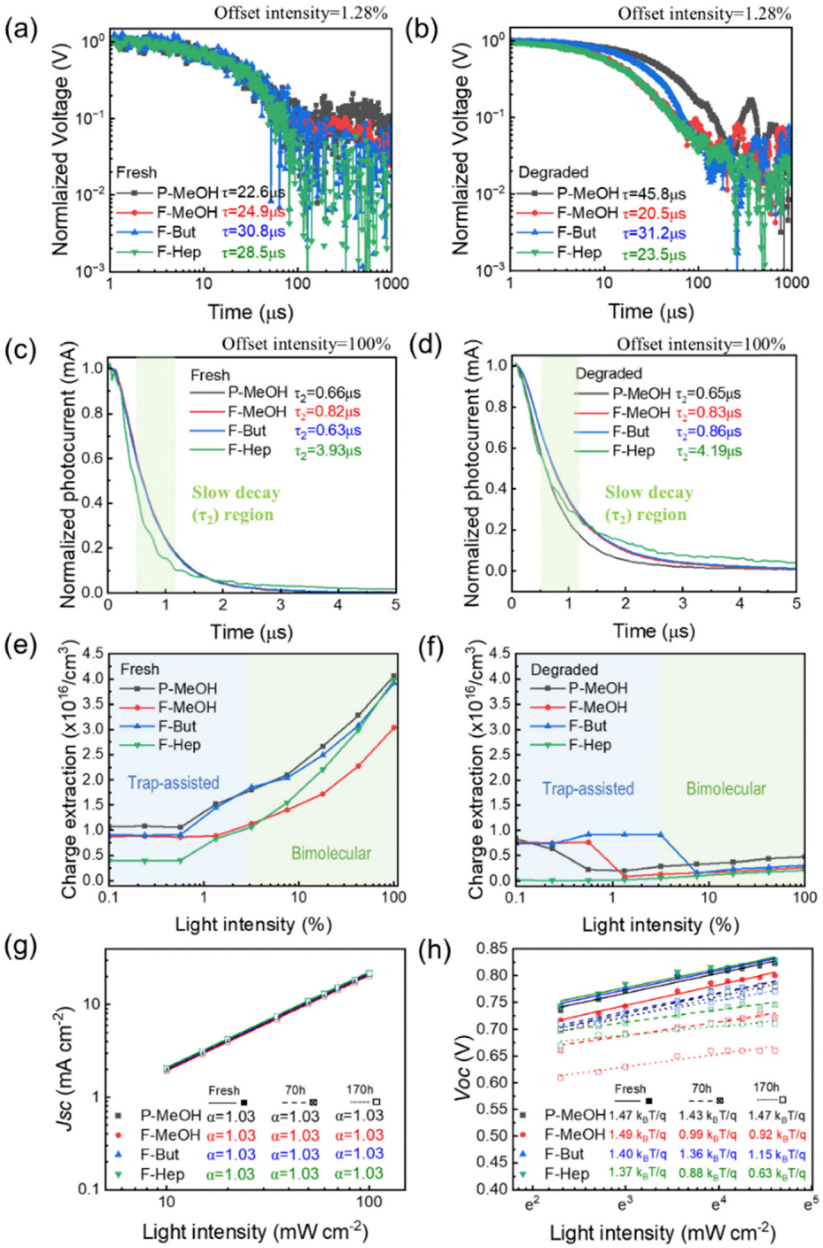

Fig. 4 TPV, TPC, and extracted charge carrier density, respectively, of (a), (c) and (e) fresh and (b), (d) and (f) degraded (under illumination with 100 mW cm^{-2} for 55 hours) devices. Light intensity-dependent (g) J_{sc} and (h) V_{oc}.

In contrast, F-Hep exhibits a critical reduction in charge extraction across all light-intensity regions, probably due to increased trap-assisted bulk or surface recombination and bimolecular recombination.

J_{sc} and V_{oc} light-intensity dependence measurements were conducted on the fresh and photodegraded (70 and 170 hours) devices to ascertain the recombination mechanisms. The J_{sc} depends on the incident light intensity, with $J_{sc} \propto I^{\alpha}$ and α typically between 0.85 and 1. An α far below 1 is attributed to nongeminate recombination. The α for all fresh and degraded devices is around 1, meaning all devices exhibit modest bimolecular recombination losses. A plot V_{oc} against the natural logarithm of the light intensity yields the ideality factor, n, typically between 1 and 2, with 1 signaling the absence of trap-assisted recombination. However, a deviation from 1 could mean severe trap-assisted bulk[19,52,53] or surface recombination[54–56] in the devices or at the BHJ layer/contact interface. All fresh devices reveal the presence of traps with n between 1.4 and 1.5, indicating that all fresh devices exhibit trap-assisted recombination, predominantly driven by possible bulk recombination. Consistent with the stability trends, the degraded devices of P-MeOH maintained their n value at 1.47 even after 170 h degradation, partly explaining their relative stability compared to F-PDIN-EH. However, n drastically dropped for F-PDIN-EH devices. The n of F-But decreased slightly from 1.40 to 1.15. The n values of F-MeOH and especially F-Hep have substantially reduced from

1.49 to 0.92 and 1.37 to 0.63, respectively, indicating an increase in surface recombination[54–56] when F-PDIN-EH is used as the interlayer, with F-Hep experiencing the worst surface recombination effect. Although this does not translate directly into a quantitative increase in the number of traps at the interface during degradation, it is a qualitative measure of the severe surface recombination upon degradation, with F-Hep devices being the most impacted. This suggests trap states are predominantly associated with interfacial defects or energetics influenced by CIL processing conditions.

To better understand the effect of CILs on device performance, particularly on V_{oc}, we conducted electrochemical impedance spectroscopy (EIS) measurements and a Mott–Schottky analysis, respectively. Fig. 5(a) and (b) show the Nyquist plot for fresh degraded devices, which includes an $R + (R + R\|C)\|C$ equivalent circuit with the series resistance (R_S), the shunt resistance (R_{Sh}), and the capacitance C (values presented in Table S3, ESI†). The arc at a low-frequency regime is associated with R_{Sh}, which relates to the charge carrier recombination. R_{Sh} of P-MeOH and F-MeOH decreases after degradation, which is normal degradation behavior with a higher leakage current that leads to charge carrier recombination. Interestingly, F-But and F-Hep exhibit much higher R_{Sh}, implying much lower leakage current in the fresh devices. These high R_{Sh} values can be attributed to the smoother surfaces observed in the AFM images. However, while R_{Sh} of F-But slightly increases for the degraded device, that of F-Hep is extremely reduced. This highlights the abnormal instability of heptane as a solvent for CILs. Fig. 5(c) and (d) show the capacitance–voltage plot measured at room temperature and a fixed frequency of 1 kHz. The built-in potential (V_{bi}) of P-MeOH, F-MeOH, F-But, and F-Hep are obtained at 0.76 V, 0.75 V, 0.73 V, and 0.75 V for fresh devices, compared to 0.74 V, 0.61 V, 0.74 V, and 0.36 V for degraded devices, respectively. These results validate the observed pronounced decrease in the V_{oc} of F-MeOH and F-Hep, especially for photo- and thermal-degraded devices (Fig. 2, Fig. S1 and S3, ESI†), reaffirming interfacial degradation (leading to increased surface recombination) as discussed earlier under the charge carrier dynamics section. Overall, we observe a reduction in the radius of the semicircles from fresh devices in Fig. 5(a) to degraded devices in Fig. 5(b), with F-Hep recording the highest reduction. This is due to the extreme decrease in R_{Sh}, highlighting the abnormal instability of F-Hep devices. Fig. 5(c) and (d) show a similar trend for F-Hep from fresh to degraded devices for the Mott–Schottky analysis, with a drastic reduction in built-in potential, V_{bi}. Both measurements reaffirm interfacial degradation with increased surface recombination as the culprit for the instability of the F-series devices. Details of the analysis can be found in the ESI,† beneath Table S3.

In addition, we probe (i) surface properties between these green solvents and PM6:Y6 films and CILs, as shown in Fig. S8 (ESI†), and (ii) interface solvent residue or chemical interaction by conducting Fourier transform infrared spectroscopy (FTIR) on fresh and aged thin CIL films on the top of PM6:Y6 film. Heptane shows the best wettability, which might contribute to the instability of F-Hep, either due to solvent residue or chemical interaction with PM6:Y6 underneath. However, it was difficult to detect any solvent residue or chemical interaction between PM6:Y6, CILs, and solvents for CILs through FTIR measurement. This finding reinforces the combined

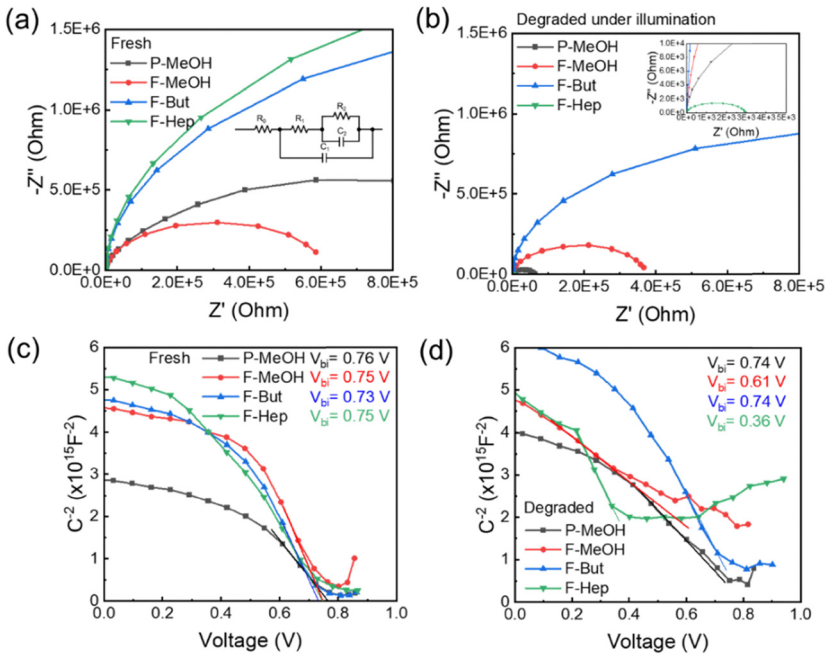

Fig. 5 Nyquist plots obtained from impedance spectroscopy (EIS) data measured across a frequency range of 10 Hz to 1 MHz for the devices with different CILs: (a) fresh devices with an inset showing the equivalent circuit for fitting, and (b) degraded devices (under illumination with 100 mW cm^{-2} for 55 hours) with an inset magnifying the lower impedance region. Mott–Schottky plots derived from capacitance–voltage (C–V) measurements at a fixed frequency of 1 kHz for (c) fresh devices and (d) degraded devices (under illumination with 100 mW cm^{-2} for 55 hours).

effects of increased surface recombination and reduced charge carrier mobility[57] as the main reasons for the severe degradation observed for F-Hep-based devices.

We further monitored the CIL-only films using Fourier transform infrared spectroscopy (FTIR) for up to 5 hours under ambient conditions to clarify the potential chemical decomposition or oxidation of the materials. First, ATR-FTIR measurements were performed on PDINO and F-PDIN-EH powders as references to easily differentiate the peaks originating from the silicon wafer substrate and those from the materials in the thin film. As illustrated in Fig. 6, the peaks at 1687 cm^{-1} correspond to imide C═O stretching in both materials. The fingerprint peaks for PDINO include aromatic C═C stretching at 1594 cm^{-1} and C–N stretching at 1351 cm^{-1}, which are likely influenced by electron-withdrawing ammonium moiety.[58] In contrast, the peak at 1300 cm^{-1} for F-PDIN-EH corresponds to C–F stretching. The fingerprint peaks are intact after 5 hours under ambient conditions. The peaks for C═O stretching slightly increased over time, which could indicate potential oxidation. In addition, an increase in O–H stretching is also observed for all the samples, as shown in Fig. S9 (ESI†). However, no new or shifted carbonyl (C═O) peaks are observed for any of the CILs, indicating no severe oxidation of these materials. In fact, PDI-based materials are generally known for their remarkable chemical, thermal, and photostability.[59,60] Note that the O–H peak in the PDINO reflects increased hydrophilicity due to the ionic group in the structure, whereas F-PDIN-EH is more hydrophobic, which is consistent with the contact angle measurement (Fig. S8, ESI†) and indicative of the chemical structure effect of the CIL materials on the devices.

The C–H peaks at around 2950 cm^{-1} in Fig. S9 (ESI†) are inverted in F-Hep, likely due to anomalous dispersion. However, this anomalous dispersion is only observed for the F-Hep film, which could be due to the solvent effect. Near vibrational resonance (like C–H stretching modes), the refractive index of the material can change rapidly, leading to a situation where the film's refractive index behaves abnormally. This can cause an increase in reflectance instead of normal absorption, creating an inverted peak in the spectrum. This effect is often seen when certain organic thin films are studied on glass or silicon substrates using FT-IR techniques.[61,62] Though we do not have a complete understanding of the exact effect of Hep on the thin film itself, compared to the rest of the films, it seems Hep changes the refractive index of the F-PDIN-EH, subsequently impacting device stability rapidly. More interestingly, we observed clear peak variation over time near 675 cm^{-1} in F-But and F-Hep, which correspond to out-of-plane C–H bending.[63] In contrast, this peak in P-MeOH and F-MeOH remains consistent. Since the out-of-plane C–H bending peak variation can be affected by molecular geometry, we hypothesize that this peak could indirectly reflect intermolecular interaction, which, in turn, influences the π–π stacking of PDI-based materials and potentially affect their charge carrier mobility.

To clarify this, we monitored the CIL films only using UV-vis-NIR spectroscopy under various conditions. Fig. 7 shows the absorption spectra of CILs at different times, up to 44 hours

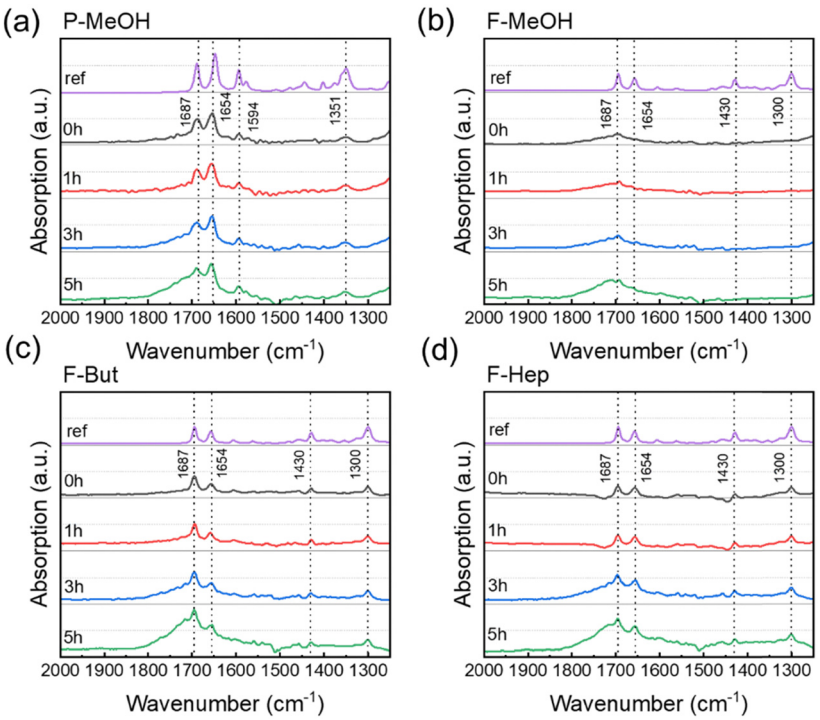

Fig. 6 Fourier transform infrared spectroscopy (FT-IR) data of CIL films measured at different times under vacuum conditions in transmission mode. The samples were stored under ambient shelf conditions for up to 5 hours: (a) P-MeOH, (b) F-MeOH, (c) F-But, and (d) F-Hep. The references are measured using ATR-FTIR on PDINO and F-PDIN-EH powders.

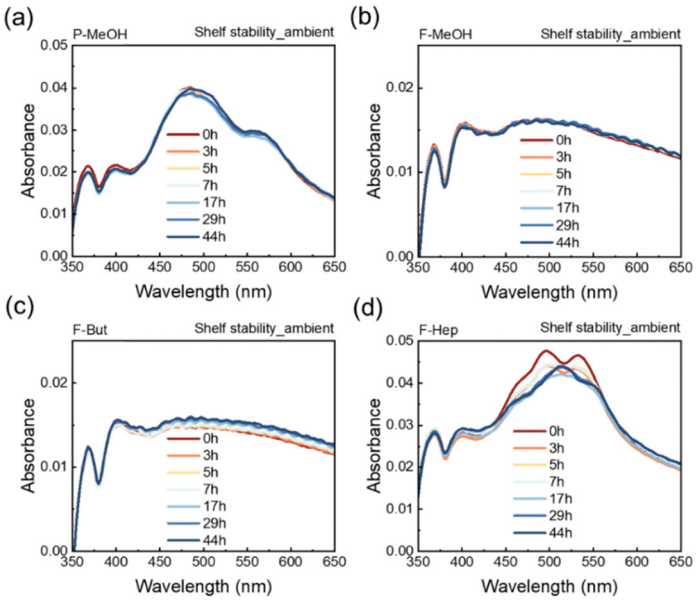

Fig. 7 Absorption spectra of the CIL thin films on a bare-glass substrate at different times under ambient conditions: (a) P-MeOH, (b) F-MeOH, (c) F-But, and (d) F-Hep.

under ambient conditions. P-MeOH exhibits a main absorption peak near 480 nm (Fig. 7(a)). The absorption peaks and shape of P-MeOH only slightly changed over 44 hours. The absorption features of F-MeOH (Fig. 7(b)) and F-But (Fig. 7(c)) are also largely maintained, although the absorption intensity of F-But slightly increases over time. F-Hep (Fig. 7(d)) showed two peaks corresponding to the 0-0 transition at 530 nm and 0-1 transition at 495 nm in the fresh sample at 0 h, as observed in the previous study.[30] However, an additional peak emerged at around 512 nm, positioned between the original peaks. This suggests the formation of defect states in the F-Hep film due to energetic disorder, which can be either due to morphological instability with H-aggregation, chemical decomposition, or oxidation.[64,65] The absorption spectra of CILs under continuous illumination and heat treatment at 85 °C are also shown in Fig. S10 (ESI†). Again, under continuous illumination, the absorption of F-Hep rapidly decreases due to its photobleaching, which contributes to the poor photostability of F-Hep-based devices with the decay in charge carrier transport, as observed earlier, due to increased recombination, especially surface recombination.

To further validate the effect of π–π stacking on device stability, we measured the electron mobility of electron-only devices with these CILs using the single-carrier space charge limited current (SCLC) method, as π–π stacking in their morphology is directly linked to crystallinity. The electron mobilities are determined by analyzing the *J*–*V* characteristics of single carrier devices under dark conditions, using the modified Mott–Gurney relation for SCLC:

$$J_{\mathrm{SCL}} = \frac{9}{8}\varepsilon_{\mathrm{r}}\varepsilon_0\mu\frac{V^2}{d^3}\exp\left(\frac{0.89\beta}{\sqrt{L}}\sqrt{V_{\mathrm{in}}}\right)$$

where J_{SCL} is the current density, μ is the carrier mobility, $\varepsilon_{\mathrm{r}}\varepsilon_0$ is the dielectric permittivity, L is the thickness of the device, and β is the field activation factor.[51]

The mobilities of the CIL-based electron-only devices were also monitored over time under illumination in N_2 to assess photostability and under ambient conditions to evaluate shelf stability. Fig. 8(a) shows the highest initial mobility in P-MeOH, followed by F-But, F-MeOH, and F-Hep in their fresh samples. This explains the relatively lower initial FF of F-MeOH and F-Hep compared to P-MeOH and F-But. Fig. 8(b) shows that the mobility of these devices increases under continuous illumination due to the light-soaking effect. After 25 hours, the mobilities stabilize, with P-MeOH showing the highest mobility, followed by F-But, F-MeOH, and F-Hep. This mobility trend is consistent with the photostability of the devices under N_2 environment, as observed earlier. The mobility values at different times in Fig. 8(b) are summarized in Table S4 (ESI†). Under ambient conditions, the mobilities reflect the solvent effect of the CILs, as shown in Fig. 8(c) and (d). The mobilities of P-MeOH and F-MeOH remain stable, whereas those of F-But and F-Hep decrease over time. These results support our previous observations from absorption and FTIR measurements that the energetic disorder and defect states and the changes in π–π stacking in these CILs with different solvents affect the charge carrier mobility of these CILs-based devices. As a result, the higher mobility of P-MeOH and F-But under continuous illumination suggests that these solvents promote well-ordered morphology and improved charge transport characteristics. In contrast, the decline in mobility for F-But and F-Hep under ambient conditions underscores the impact of morphological and interfacial instability of these CILs. These changes in mobility point to an imbalance in charge carrier transport (directly linked to the FF) and increased surface recombination, which are reflected in the severe degradation of the F-PDIN-EH-based devices compared to the less degradation of PDINO-based devices, highlighting the chemical structure effect on the device

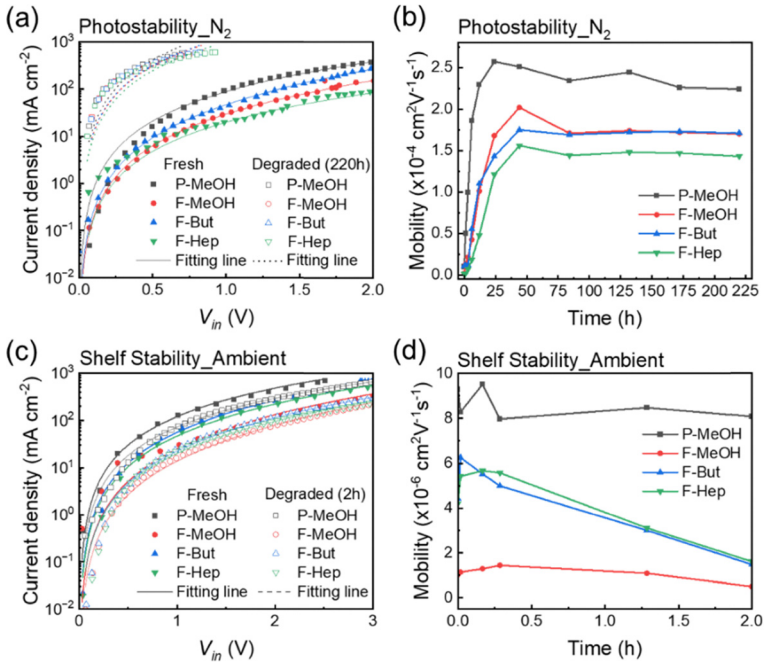

Fig. 8 Dark J–V characteristics of fresh and degraded electron-only devices and average mobilities of electron-only devices (n = 6) with different CILs stored under different conditions: (a) and (b) under continuous illumination in N2 up to 220 hours; (c) and (d) under ambient shelf condition up to 2 hours.

stability. Finally, the continuous drastic decrease in mobility of F-Hep-based devices compared to F-MeOH and F-But-based devices, as shown in Fig. S11 (Fig. S11b, ESI†), cements the processing solvent effect on the stability of the devices.

Conclusions

We have shown that the chemical structure of the CIL material and its processing solvent affect the performance of OSCs, especially their stability. This is one of the first investigations into the effect of non-polar CIL solvents on device stability. We showed that transitioning from traditionally well-established CIL material, in this case, self-doped PDINO, to a chemically designed "to be stable" material, F-PDIN-EH, may not readily result in efficient and stable devices. Our results reveal that devices with F-MeOH and F-Hep experience severe degradation over time, whereas devices with F-But and P-MeOH exhibit relatively better stability. The degradation mechanisms in devices with these CILs are analyzed through in-depth TPV, TPC, extracted charge carrier density, and light intensity dependence of J_{sc} and V_{oc} measurements. Further studies using absorption spectroscopy, FTIR, and mobility measurements confirmed that although the CIL films themselves are chemically stable to a certain extent, the degradation in these CILs is most likely caused by energetic disorder and imbalanced charge transport. These findings suggest that the degradation of the devices with F-PDIN-EH is most likely due to surface recombination. The degradation in F-Hep, especially, appears to result from severe charge carrier imbalance due to morphological instability in π–π stacking, resulting in both trap-assisted and surface recombination, thus, drastic loss in FF. In contrast, F-But shows higher electron mobility, contributing to improved device stability.

Additionally, we have observed that optimizing the device stack could improve the performance, as revealed by the comparative photostability under a nitrogen environment of optimized and unoptimized CIL layers. Thus, transitioning traditional processing solvents to eco-friendly solvents for high performance must align with efforts for good solubility, layer formation, acceptable energetics, balanced charge transport, and reduced charge carrier recombination. With the CILs case study, it is evident that the OSC community must improve the fabrication process and device optimization, targeting recently designed or existing materials for greener solution-processed OSC technology and sustainability.

Experimental methods

Materials

Unless otherwise specified, most materials and solvents were sourced from Sigma-Aldrich. In addition, PM6, Y6, and PDINO were purchased from 1-material, while PEDOT:PSS (AI4083) was supplied by Heraeus. F-PDIN-EH was synthesized and provided by our collaborators from the Advanced Functional Materials and Coatings Laboratory at the University of Calgary, as recently detailed in their work.[30] Chloroform was purchased from VWR.

Device fabrication

Solar cells were fabricated following a multilayer stack structure: glass/ITO/PEDOT:PSS (~40 nm)/PM6:Y6 (~100 nm)/CILs/Ag (~100 nm). The ITO-coated glass substrates (12–20 Ω sq^{-1}, sourced from Colorado Concept Coating LLC) were sequentially

cleaned, with ultrasonication for 15 minutes each, in a deionized soap, acetone, and isopropanol. They were dried at 120 °C for 10 minutes and UV-ozone treated for 20 minutes. PEDOT:PSS was spin-coated onto the substrates as HTL at 2000 rpm for 40 s, followed by annealing at 120 °C for 10 minutes in air. The PM6:Y6 active layer (1 : 1.2 ratio, 16 mg mL^{-1} in chloroform) was deposited under a nitrogen environment without additives or thermal annealing. CIL solutions were then prepared as follows: 1.0 mg mL^{-1} PDINO in methanol, 0.5 mg mL^{-1} F-PDIN-EH in methanol, 1.0 mg mL^{-1} F-PDIN-EH in 1-butanol, and 1.0 mg mL^{-1} F-PDIN-EH in heptane and spin-coated onto the active layer at 2500 rpm for 40 s. Finally, a 100 nm layer of Ag was thermally evaporated atop the CILs. Electron-only devices were fabricated with the following structure: glass/ITO/SnO_2/PM6:Y6 (~100 nm)/CILs/Ag (~100 nm). The devices were measured in the dark while being stored under different environmental conditions.

Characterizations

Bruker Icon II was used for AFM measurement using a ScanAsyst AIR probe with peak force tapping mode. Contact angle measurement was performed using an Ossila contact angle goniometer. The *J–V* characteristics were measured with a Keithley 4200 source meter for the OSCs under simulated 100 mW cm^{-2} AM 1.5 G solar radiation and Fluxim Litos-Lite setup. This radiation was generated by a 450 W xenon lamp (Oriel Sol 2A Class ABA), calibrated with a reference silicon cell covered by KG5-filtered glass. For each device type, the *J–V* characteristics were taken for 10 to 15 devices, and their PV parameters were obtained with their best and average values shown in Table 1. The stability and light intensity dependent J_{sc} and V_{oc} measurement of the OSCs were evaluated using the Litos Lite setup equipped with a Wavelabs Sinus LS2 solar simulator with AM 1.5 spectrum. The stability measurements were conducted according to ISOS protocols: ISOS-D-1 for shelf stability (dark, open circuit, and at room temperature), ISOS-L-1 for photostability (illumination at 1 sun, open circuit, and room temperature), and ISOS-T-1 for thermal stability (dark, open circuit, and at 85 °C). Fluxim AG Paios system with white LED light was used to carry out the TPC, TPV, capacitance–voltage (Mott–Schottky analysis), and EIS measurements. The dark *J–V* measurement of the electron-only devices was carried out using a Fluxim AG Litos-Lite setup.

For absorption measurements, the CILs were spin-coated at 800 rpm for 40 seconds onto bare glass substrates and measured using a LAMBDA 1050+ UV/vis/NIR spectroscopy with 2 nm increments. FTIR measurements were performed on CIL films spin-coated at 800 rpm for 40 seconds onto silicon wafers in transmission mode using a Bruker VERTEX 80 V spectrometer equipped with a mid-band liquid nitrogen-cooled mercury cadmium telluride (MCT) detector. Measurements were taken at normal incidence as an average of 16 570 scans (15-minute acquisitions) at 4 cm^{-1} resolution, and absorbance was calculated by referencing a clean bare silicon wafer (300 μm thick, double-side polished, undoped). All measurements were conducted under vacuum to mitigate water vapor and CO_2 intrusion. Powder spectra were collected on a Bruker VERTEX 70 spectrometer equipped with a mid-band MCT detector, and a Harrick VariGATR attenuated total reflection (ATR) germanium accessory at an incident angle of 60 degrees. A total of 500 scans were averaged at 4 cm^{-1} resolution, and absorbance was calculated by referencing a clean bare Ge crystal. The CIL-only films for absorption and FTIR were dried under vacuum for 10–15 minutes before measurement.

Author contributions

Souk Y. Kim: data curation, investigation, methodology, supervision, formal analysis, visualization, writing – original draft, and writing – review & editing; Pimmada Sawangwong: data curation, investigation, formal analysis, and validation; Colton Atkinson: investigation, resources, and formal analysis; Gregory Welch: formal analysis, supervision, funding acquisition, and writing – review & editing; and Nutifafa Y. Doumon: conceptualization, data curation, formal analysis, investigation, methodology, project administration, supervision, validation, visualization, writing – original draft, and writing – review & editing.

Data availability

Part of the data supporting this article has been included in the ESI.† All other data in this study will be made available upon request from the corresponding author.

Conflicts of interest

The authors declare no conflict of interest.

Acknowledgements

S. Y. Kim acknowledges Dr Asuo for valuable discussions on data acquisition and analysis from the Fluxim AG Paios system, especially the TPV, TPC, and EIS. S. Y. Kim and N. Y. Doumon acknowledge Penn State Materials Characterization Lab for the use of the Bruker Icon II AFM and Bruker Vertex 70 FTIR and staff Dr Zimudzi for helpful discussions on sample preparation and FTIR measurements and results discussion. N. Y. Doumon acknowledges support from the Penn State Materials Research Institute, enabling access to the AFM and FTIR characterization tools. N. Y. Doumon acknowledges funding support from the Penn State Institute of Energy and the Environment. C. Atkinson and G. C. Welch thank the University of Calgary and the NSERC DG program (2019-04392) for infrastructure and funding support, respectively.

References

1 R. Adel Abdelaleim, G. Morse, F. Silvestri, E. Barrena, E. Martinez Ferrero, M. Campoy Quiles, P. Tiwana and M. Stella, *Sol. Energy Mater. Sol. Cells*, 2022, **245**, 111852.
2 D. Lv, Q. Jiang, Y. Shang and D. Liu, *npj Flexible Electron.*, 2022, **6**, 38.

3 F. Zhao, J. Zhou, D. He, C. Wang and Y. Lin, *J. Mater. Chem. C*, 2021, **9**, 15395–15406.
4 H. Fu, J. Yao, M. Zhang, L. Xue, Q. Zhou, S. Li, M. Lei, L. Meng, Z.-G. Zhang and Y. Li, *Nat. Commun.*, 2022, **13**, 3687.
5 S. Y. Kim, N. Rayes, A. R. Kemanian, E. D. Gomez and N. Y. Doumon, *Energy Adv.*, 2025, **4**, 37–54.
6 R. H. E. Hassanien, M. Li and F. Yin, *Renewable Energy*, 2018, **121**, 377–388.
7 M. Kaltenbrunner, M. S. White, E. D. Głowacki, T. Sekitani, T. Someya, N. S. Sariciftci and S. Bauer, *Nat. Commun.*, 2012, **3**, 770.
8 J. Panidi, D. G. Georgiadou, T. Schoetz and T. Prodromakis, *Adv. Funct. Mater.*, 2022, **32**, 2200694.
9 R. Suthar, H. Dahiya, S. Karak and G. D. Sharma, *J. Mater. Chem. C*, 2023, **11**, 12486–12510.
10 X. Liu, S. Xu, B. Tang and X. Song, *Chem. Eng. J.*, 2024, **497**, 154944.
11 S. Feroze, A. Distler, K. Forberich, I. Ahmed Channa, B. Doll, C. J. Brabec and H.-J. Egelhaaf, *Sol. Energy*, 2023, **263**, 111894.
12 S. Feroze, A. Distler, L. Dong, M. Wagner, I. A. Channa, F. Hoga, C. J. Brabec and H.-J. Egelhaaf, *Energy Environ. Sci.*, 2025, **18**, 674–688.
13 L. Duan, B. Hoex and A. Uddin, *Sol. RRL*, 2021, **5**, 2100041.
14 Z. Chen, J. Ge, W. Song, X. Tong, H. Liu, X. Yu, J. Li, J. Shi, L. Xie, C. Han, Q. Liu and Z. Ge, *Adv. Mater.*, 2024, **36**, 2406690.
15 J. Wang, Z. Zheng, P. Bi, Z. Chen, Y. Wang, X. Liu, S. Zhang, X. Hao, M. Zhang, Y. Li and J. Hou, *Natl. Sci. Rev.*, 2023, **10**, nwad085.
16 Z. Zheng, J. Wang, P. Bi, J. Ren, Y. Wang, Y. Yang, X. Liu, S. Zhang and J. Hou, *Joule*, 2022, **6**, 171–184.
17 Heliatek achieves ICE 61215 certification for lightweight and flexible HeliaSol solar film, **https://ope-journal.com/news/heliatek-achieves-ice-61215-certification-for-lightweight-and-flexible-heliasol-solar-film**, (accessed October 10, 2024).
18 N. Y. Doumon and L. J. A. Koster, *Sol. RRL*, 2019, **3**, 1800301.
19 N. Y. Doumon, G. Wang, R. C. Chiechi and L. J. A. Koster, *J. Mater. Chem. C*, 2017, **5**, 6611–6619.
20 N. Y. Doumon, F. V. Houard, J. Dong, H. Yao, G. Portale, J. Hou and L. J. A. Koster, *Org. Electron.*, 2019, **69**, 255–262.
21 A. Classen, T. Heumueller, I. Wabra, J. Gerner, Y. He, L. Einsiedler, N. Li, G. J. Matt, A. Osvet, X. Du, A. Hirsch and C. J. Brabec, *Adv. Energy Mater.*, 2019, **9**, 1902124.
22 Y. Dong, Y. Zou, J. Yuan, H. Yang, Y. Wu, C. Cui and Y. Li, *Adv. Mater.*, 2019, **31**, 1904601.
23 D. Zhou, L. Han, L. Hu, S. Yang, X. Shen, Y. Li, Y. Tong, F. Wang, Z. Li and L. Chen, *ACS Appl. Mater. Interfaces*, 2023, **15**, 8367–8376.
24 F. Qin, W. Wang, L. Sun, X. Jiang, L. Hu, S. Xiong, T. Liu, X. Dong, J. Li, Y. Jiang, J. Hou, K. Fukuda, T. Someya and Y. Zhou, *Nat. Commun.*, 2020, **11**, 4508.
25 J. Wang, R. Peng, J. Gao, D. Li, L. Xie, W. Song, X. Zhang, Y. Fu and Z. Ge, *ACS Appl. Mater. Interfaces*, 2021, **13**, 45789–45797.
26 S. Dong, Z. Hu, K. Zhang, Q. Yin, X. Jiang, F. Huang and Y. Cao, *Adv. Mater.*, 2017, **29**, 1701507.
27 D. Di Carlo Rasi, P. M. J. G. van Thiel, H. Bin, K. H. Hendriks, G. H. L. Heintges, M. M. Wienk, T. Becker, Y. Li, T. Riedl and R. A. J. Janssen, *Sol. RRL*, 2019, **3**, 1800366.
28 Z.-G. Zhang, B. Qi, Z. Jin, D. Chi, Z. Qi, Y. Li and J. Wang, *Energy Environ. Sci.*, 2014, **7**, 1966–1973.
29 R. Sorrentino, E. Kozma, S. Luzzati and R. Po, *Energy Environ. Sci.*, 2021, **14**, 180–223.
30 C. Atkinson, M. R. Niazi and G. C. Welch, *RSC Appl. Interfaces*, 2024, **1**, 245–251.
31 J. Yao, Q. Chen, C. Zhang, Z.-G. Zhang and Y. Li, *SusMat*, 2022, **2**, 243–263.
32 M. Zhang, Y. Bai, C. Sun, L. Xue, H. Wang and Z.-G. Zhang, *Sci. China: Chem.*, 2022, **65**, 462–485.
33 X. Ma, J. Wang, J. Gao, Z. Hu, C. Xu, X. Zhang and F. Zhang, *Adv. Energy Mater.*, 2020, **10**, 2001404.
34 J. Yao, B. Qiu, Z. G. Zhang, L. Xue, R. Wang, C. Zhang, S. Chen, Q. Zhou, C. Sun, C. Yang, M. Xiao, L. Meng and Y. Li, *Nat. Commun.*, 2020, **11**, 2726.
35 Y. Lin, A. Magomedov, Y. Firdaus, D. Kaltsas, A. El-Labban, H. Faber, D. R. Naphade, E. Yengel, X. Zheng, E. Yarali, N. Chaturvedi, K. Loganathan, D. Gkeka, S. H. AlShammari, O. M. Bakr, F. Laquai, L. Tsetseris, V. Getautis and T. D. Anthopoulos, *ChemSusChem*, 2021, **14**, 3569–3578.
36 Z.-G. Zhang, B. Qi, Z. Jin, D. Chi, Z. Qi, Y. Li and J. Wang, *Energy Environ. Sci.*, 2014, **7**, 1966–1973.
37 J. Yuan, Y. Zhang, L. Zhou, G. Zhang, H. L. Yip, T. K. Lau, X. Lu, C. Zhu, H. Peng, P. A. Johnson, M. Leclerc, Y. Cao, J. Ulanski, Y. Li and Y. Zou, *Joule*, 2019, **3**, 1140–1151.
38 J. Yao, S. Ding, R. Zhang, Y. Bai, Q. Zhou, L. Meng, E. Solano, J. A. Steele, M. B. J. Roeffaers, F. Gao, Z.-G. Zhang and Y. Li, *Adv. Mater.*, 2022, **34**, 2203690.
39 W. Zhang, G. Zhang, H. Song, S. Kim, H. Chen, C. Yang, Y. Zhang, K. Yang and S. Lu, *Sol. RRL*, 2023, **7**, 2201076.
40 L. Tian, Q. Xue, Z. Hu and F. Huang, *Org. Electron.*, 2021, **93**, 106141.
41 R. D. Pettipas, A. Hoff, B. S. Gelfand and G. C. Welch, *ACS Appl. Mater. Interfaces*, 2022, **14**, 3103–3110.
42 C. Song, X. Liu, X. Li, Y.-C. Wang, L. Wan, X. Sun, W. Zhang and J. Fang, *ACS Appl. Mater. Interfaces*, 2018, **10**, 14986–14992.
43 M. O. Reese, S. A. Gevorgyan, M. Jørgensen, E. Bundgaard, S. R. Kurtz, D. S. Ginley, D. C. Olson, M. T. Lloyd, P. Morvillo, E. A. Katz, A. Elschner, O. Haillant, T. R. Currier, V. Shrotriya, M. Hermenau, M. Riede, K. R. Kirov, G. Trimmel, T. Rath, O. Inganäs, F. Zhang, M. Andersson, K. Tvingstedt, M. Lira-Cantu, D. Laird, C. McGuiness, S. (Jimmy) Gowrisanker, M. Pannone, M. Xiao, J. Hauch, R. Steim, D. M. DeLongchamp, R. Rösch, H. Hoppe, N. Espinosa, A. Urbina, G. Yaman-Uzunoglu, J.-B. Bonekamp, A. J. J. M. van Breemen, C. Girotto, E. Voroshazi and F. C. Krebs, *Sol. Energy Mater. Sol. Cells*, 2011, **95**, 1253–1267.
44 M. V. Khenkin, E. A. Katz, A. Abate, G. Bardizza, J. J. Berry, C. Brabec, F. Brunetti, V. Bulović, Q. Burlingame, A. Di Carlo, R. Cheacharoen, Y.-B. Cheng, A. Colsmann, S. Cros, K. Domanski, M. Dusza, C. J. Fell, S. R. Forrest, Y. Galagan, D. Di Girolamo, M. Grätzel, A. Hagfeldt, E. von Hauff, H. Hoppe, J. Kettle, H. Köbler, M. S. Leite, S. (Frank) Liu,

Y.-L. Loo, J. M. Luther, C.-Q. Ma, M. Madsen, M. Manceau, M. Matheron, M. McGehee, R. Meitzner, M. K. Nazeeruddin, A. F. Nogueira, Ç. Odabaşı, A. Osherov, N.-G. Park, M. O. Reese, F. De Rossi, M. Saliba, U. S. Schubert, H. J. Snaith, S. D. Stranks, W. Tress, P. A. Troshin, V. Turkovic, S. Veenstra, I. Visoly-Fisher, A. Walsh, T. Watson, H. Xie, R. Yıldırım, S. M. Zakeeruddin, K. Zhu and M. Lira-Cantu, *Nat. Energy*, 2020, **5**, 35–49.

45 L. Meng, C. Sun, R. Wang, W. Huang, Z. Zhao, P. Sun, T. Huang, J. Xue, J.-W. Lee, C. Zhu, Y. Huang, Y. Li and Y. Yang, *J. Am. Chem. Soc.*, 2018, **140**, 17255–17262.

46 I. M. Asuo, A. M. Varposhti, E. D. Gomez and N. Y. Doumon, *J. Mater. Chem. C*, 2024, **12**, 7562–7571.

47 B. C. O'Regan and F. Lenzmann, *J. Phys. Chem. B*, 2004, **108**, 4342–4350.

48 A. Maurano, R. Hamilton, C. G. Shuttle, A. M. Ballantyne, J. Nelson, B. O'Regan, W. Zhang, I. McCulloch, H. Azimi, M. Morana, C. J. Brabec and J. R. Durrant, *Adv. Mater.*, 2010, **22**, 4987–4992.

49 N. Kudo, K. Uchida, T. Ikoma, K. Takahashi, D. Kuzuhara, M. Suzuki, H. Yamada, D. Kumagai, Y. Yamaguchi and K.-I. Nakayama, *Sol. RRL*, 2018, **2**, 1700234.

50 W. Yang, W. Wang, Y. Wang, R. Sun, J. Guo, H. Li, M. Shi, J. Guo, Y. Wu, T. Wang, G. Lu, C. J. Brabec, Y. Li and J. Min, *Joule*, 2021, **5**, 1209–1230.

51 J. Min, Y. N. Luponosov, N. Gasparini, M. Richter, A. V. Bakirov, M. A. Shcherbina, S. N. Chvalun, L. Grodd, S. Grigorian, T. Ameri, S. A. Ponomarenko and C. J. Brabec, *Adv. Energy Mater.*, 2015, **5**, 1500386.

52 N. Y. Doumon, M. V. Dryzhov, F. V. Houard, V. M. Le Corre, A. Rahimi Chatri, P. Christodoulis and L. J. A. Koster, *ACS Appl. Mater. Interfaces*, 2019, **11**, 8310–8318.

53 Q. Bao, O. Sandberg, D. Dagnelund, S. Sandén, S. Braun, H. Aarnio, X. Liu, W. M. Chen, R. Österbacka and M. Fahlman, *Adv. Funct. Mater.*, 2014, **24**, 6309–6316.

54 V. V. Brus, *Org. Electron.*, 2016, **29**, 1–6.

55 S. Wheeler, F. Deledalle, N. Tokmoldin, T. Kirchartz, J. Nelson and J. R. Durrant, *Phys. Rev. Appl.*, 2015, **4**, 024020.

56 J. Reinhardt, M. Grein, C. Bühler, M. Schubert and U. Würfel, *Adv. Energy Mater.*, 2014, **4**, 1400081.

57 S. B. Hacène and T. Benouaz, *Phys. Status Solidi A*, 2014, **211**, 862–868.

58 S. Ogi, V. Stepanenko, K. Sugiyasu, M. Takeuchi and F. Würthner, *J. Am. Chem. Soc.*, 2015, **137**, 3300–3307.

59 H. Sun and Q. Zhang, *ChemPhotoChem*, 2024, **8**, e202300213.

60 Y. Li, X. Zhang and D. Liu, *J. Photochem. Photobiol., C*, 2021, **48**, 100436.

61 Y. S. Yen and J. S. Wong, *J. Phys. Chem.*, 1989, **93**, 7208–7216.

62 M. Song, J.-W. Kang, D.-H. Kim, J.-D. Kwon, S.-G. Park, S. Nam, S. Jo, S. Yoon Ryu and C. Su Kim, *Appl. Phys. Lett.*, 2013, **102**, 143303.

63 G. Socrates, *Infrared and Raman Characteristic Group Frequencies: Tables and Charts*, Wiley, 3rd edn, 2024.

64 M. Dehghani Sanij, A. Bahrampour and A. R. Bahrampour, *Photonic Sens.*, 2019, **9**, 60–68.

65 K. Cai, J. Xie, D. Zhang, W. Shi, Q. Yan and D. Zhao, *J. Am. Chem. Soc.*, 2018, **140**, 5764–5773.